ADVANCED ENGINEERING MATERIALS

COMMUNICATION

DOI: 10.1002/adem.201500391

On Validity of Axisymmetric Assumption for Modeling an Industrial Scale Electroslag Remelting Process**

By *Ebrahim Karimi-Sibaki, Abdellah Kharicha, Jan Bohacek, Menghuai Wu** and *Andreas Ludwig*

A full 3D simulation of an industrial scale electroslag remelting (ESR) process (ϕ 750 mm ingot) is performed, and results are verified by experiment. A typical non-axis symmetry flow pattern and temperature field in the slag region is demonstrated. A statistical analysis of the turbulent flow in the slag and melt pool is performed to quantitatively characterize the transient behavior of the flow. By comparing the 3D calculation with a 2D axis-symmetrical calculation, we find that the predicted shape of melt pool (profile of the solidifying mushy zone of the ingot) are quite similar, leading to the conclusion that a 2D calculation is sufficient to solve the melt pool profile of the ingot.

Over past decades, a number of studies have been performed to model the ESR process containing the complex interaction between turbulent flow, heat, and electromagnetic fields.[1] Choudhary and Szekely[2] used the vorticity transport equation to calculate the velocity field only in the slag. Nevertheless, they calculated the temperature field both in the slag and ingot, focusing on the effect of ingot size (ϕ 100 or 660 mm). They found that the temperature field in the slag appeared to be more uniform in large-scale units. Jardy et al.[3] studied the flow and temperature fields only in the slag zone for an industrial scale ESR (ϕ 500 mm ingot). Their model predicted that a higher melt rate could be achieved when the buoyancy force is stronger than the Lorentz force in the slag region. Kelkar et al.[4] proposed a coupled model for flow, temperature, and electromagnetic fields in the slag and ingot (ϕ 470 mm) at steady state conditions. Patel[5] presented results based on an analytical model for electromagnetic distribution in ESR (ϕ 430 mm). A parabolic variation between the voltage drop across the slag and electrode diameter was predicted. Kharicha et al. developed a series of models with different focuses to investigate, for example, the shape and stability of the slag–pool interface,[6] the effect of applied frequency,[7] the importance of electric current flowing through the mold,[8] the interaction between released Joule heating and temperature fluctuation in the slag,[9] and the effect of slag–pool interface movement on solidification of the ingot.[10] Weber et al.[11] studied the effect of electrode fill ratio on the melt rate of the electrode and the liquid pool volume (ϕ 500 mm ingot). They reported a higher melt rate and larger liquid pool volume in the case with a lower electrode fill ratio. Eickhoff et al.[12] studied air gap formation due to shrinkage of a solidifying ESR ingot (ϕ 100 mm). Using a prescribed parabolic temperature distribution, radial contraction was calculated in the fully solidified ingot. Fezi et al.[13] proposed a numerical model to investigate the effects of process parameters, such as ingot diameter (ϕ 508–762 mm ingots) and the initial composition of the alloy, on macrosegregation of alloy 625.

All of the above mentioned calculations were performed in a 2D axisymmetric domain because of the limitation of the computational resources. Generally speaking, dealing with the governing equations of flow, heat transfer, or electromagnetism in 2D is simple, whereas only limited work has been attempted in 3D. One example shown by Kharicha et al.[14] modeled the effects of slag-pool interface movement, formation, departure, and dripping of droplets through the slag for an industrial scale (ϕ 600 mm ingot) ESR process. The interaction between flow and electromagnetic field was found to generate a strong 3D flow, which could not be predicted by typical 2D models. Recently, Wang et al.[15] established a 3D model to investigate a laboratory scale ESR process (ϕ 120 mm ingot). The multiphase volume of fluid (VOF) approach was used to model the melting of electrodes with the formation of droplets as well as slag pool interface

[*] *Prof. M. Wu, E. Karimi-Sibaki, Dr. A. Kharicha*
Christian Doppler Laboratory for Advanced Process Simulation of Solidification and Melting, Department of Metallurgy, University of Leoben, Franz-Josef-Str. 18, A-8700 Leoben, Austria
Dr. A. Kharicha, Dr. J. Bohacek, Prof. M. Wu, Prof. A. Ludwig
Chair of Simulation and Modeling of Metallurgical Processes, Department of Metallurgy, University of Leoben, Franz-Josef-Str. 18, A-8700 Leoben, Austria
E-mail: menghuai.wu@unileoben.ac.at

[**] *The authors acknowledge financial support from the Austrian Federal Ministry of Economy, Family, and Youth and the National Foundation for Research, Technology, and Development within the framework of the Christian Doppler Laboratory for Advanced Process Simulation of Solidification and Melting.*

movement. This type of calculation is computationally costly. For instance, the calculation performed by Kharicha et al.[14] took six months using a multi-CPU cluster (24 cores, parallel computing) for only 5 s of process even without including the solidification of the ingot. Therefore, it is not computationally feasible to include all of these phenomena, such as interface movement and droplet formation, in the industry process in 3D.

Herein, a different 3D modeling concept is proposed that focuses on an industrial scale AC electroslag remelting process by including solidification of the ingot. The governing equations are solved using the commercial CFD software FLUENT-ANSYS v.14.5, which is based on the finite volume method (FVM). The modeling equations and corresponding boundary conditions are implemented using user-defined functions (UDF). Table 1 describes all of the governing equations regarding fluid flow, heat transfer, and electromagnetism. The thermal and electrical boundary conditions are summarized in Table 2. Note that industrial measurements of material properties that are temperature dependent are used for our simulations. Table 3 lists the averaged material properties of the slag and steel as well as process parameters. The slag–pool interface is assumed to be stationary. The effect of droplets passing through the slag on the global

Table 1. Governing equations of flow, electromagnetic, and temperature fields.

Governing equations	Symbols
1. Electromagnetic field $\frac{\partial B_\theta}{\partial t}+\left[\frac{\partial}{\partial z}\left(\frac{1}{\sigma\mu_0}\frac{\partial B_\theta}{\partial z}\right)+\frac{\partial}{\partial r}\left(\frac{1}{r\sigma\mu_0}\frac{\partial(rB_\theta)}{\partial r}\right)\right]=0$ $\tilde{\vec{j}}=\frac{1}{\mu_0}(\vec{\nabla}\times\vec{B}_\theta)$	Magnetic induction (B_θ), Mag. Perm. constant (μ_0), Elec. Cond. (σ), Radial distance (r), Axial distance (z), Time (t), Current density (j)
2. Flow field $\frac{\partial\rho}{\partial t}+\nabla\cdot(\rho\vec{u})=0$ $\frac{\partial}{\partial t}(\rho\vec{u})+\nabla\cdot(\rho\vec{u}\vec{u})=-\nabla p+\nabla\cdot(\mu_{\text{eff}}(\nabla\vec{u}+\nabla\vec{u}^t))+\rho_0\vec{g}\beta(T-T_0)+\vec{F}_P+\vec{F}_L$ $\vec{F}_L=Re(\frac{1}{2}\tilde{\vec{j}}\times\vec{B}_{\theta\text{Conjugate}})$. $\vec{u}_m=f\vec{u}_l+(1-f)\vec{u}_s$ $\vec{u}_r=(\vec{u}_m-\vec{u}_s)$ $F_{\parallel}=-\frac{\mu}{K_{\parallel}}(\vec{u}_r\cdot\vec{n}_{\parallel})$ $F_{\perp}=-\frac{\mu}{K_{\perp}}(\vec{u}_r\cdot\vec{n}_{\perp})$ $\vec{F}_p=(F_{\perp})\vec{n}_{\perp}+(F_{\parallel})\vec{n}_{\parallel}$ $K_{\parallel}=\begin{cases}3.75\times10^{-4}f^2{d_1}^2 & 0<f\le0.65\\ 2.05\times10^{-7}\left[\frac{f}{1-f}\right]^{10.739}{d_1}^2 & 0.65\le f\le0.75\\ 0.074\left(\ln(1-f)^{-1}-1.49+2(1-f)-0.5(1-f)^2\right)d_1^2 & 0.75\le f<1.0\end{cases}$ $K_{\perp}=\begin{cases}1.09\times10^{-3}f^{3.32}{d_1}^2 & 0<f\le0.65\\ 4.04\times10^{-6}\left[\frac{f}{1-f}\right]^{6.7336}{d_1}^2 & 0.65\le f\le0.75\\ \left[-6.49\times10^{-2}+5.43\times10^{-2}\left[\frac{f}{1-f}\right]^{0.25}\right]{d_1}^2 & 0.75\le f\le1.0\end{cases}$ Turbulence: scale-adaptive simulation (SAS) model.[19]	Velocity (u), Density (ρ), Pressure (P), Effective viscosity (μ_{eff}), Gravity (g), Therm. expan. coeff. (β), Temperature (T), Lorentz force (F_L), Casting velocity (u_s), Liquid velocity (u_l), Mixture liquid-solid velocity (u_m), Relative velocity (u_r), Perpendicular drag force ($F_{\parallel}$), Parallel unit vector ($n_{\parallel}$), Perpendicular unit vector ($n_{\perp}$), Mushy zone drag force (F_P), Liquid fraction (f), Primary dendrite arm space (d_1), Parallel perm. ($K_{\parallel}$), Perpendicular perm. ($K_{\perp}$),
3. Temperature field and solidification $\frac{\partial}{\partial t}(\rho h)+\nabla\cdot(\rho\vec{u}h)=\nabla\cdot(\lambda_{\text{eff}}\nabla T)+Q+S_{\text{LH}}$ $Q=Re\left(\frac{1}{2\sigma}\tilde{\vec{j}}\times\tilde{\vec{j}}_{\theta\,\text{Conjugate}}\right)$ $S_{\text{LH}}=-\frac{\partial}{\partial t}(\rho fL)-\rho L\vec{u}_s\nabla f$ $f=\begin{cases}1 & T>T_{\text{liquidus}}\\ 1-\left[(T_{\text{liquidus}}-T)/\left((T_f-T)(1-k_p)\right)\right] & T_{\text{solidus}}<T\le T_{\text{liquidus}}\\ 0 & T\le T_{\text{solidus}}\end{cases}$	Enthalpy (h), Effective therm. cond. (λ_{eff}), Joule heating (Q), Latent heat (S_{LH}), Enthalpy of fusion (L), Partition coeff. (k_p), Liquidus temp. (T_{liquidus}), Solidus temp. (T_{solidus}), Melting temp. of solvent (T_f),

COMMUNICATION

Table 2. Electromagnetic and thermal boundary conditions.

Boundaries (labeled in Figure 1a)	Electromagnetic	Thermal
1. Electrode tip–slag	Coupled	$T = T_{liquidius}$
2. Electrode edge–slag	Coupled	$T = T_{liquidius}$
3. Slag–air	$B_\theta = \frac{\mu_0 I_0}{2\pi r}$	$\varepsilon = 0.8$, $H = 50\,W\,m^{-2}\,K^{-1}$
4. Electrode-air	$B_\theta = \frac{\mu_0 I_0}{2\pi r}$	Zero flux
5. Electrode top	Zero flux	$T = 900$ K
6. Mold–air	$B_\theta = \frac{\mu_0 I_0}{2\pi r}$	Zero flux
7. Mold top	$B_\theta = \frac{\mu_0 I_0}{2\pi r}$	Zero flux
8. Mold bottom	$B_\theta = \frac{\mu_0 I_0}{2\pi r}$	Zero flux
9. Mold–water	$B_\theta = \frac{\mu_0 I_0}{2\pi r}$	$H = 700\,W\,m^{-2}\,K^{-1}$
10. Slag–mold	Coupled	$H = 500\,W\,m^{-2}\,K^{-1}$
11. Slag–pool	Coupled	Coupled
12. Ingot–mold	Coupled	$H = 500\,W\,m^{-2}\,K^{-1}$
13. Air gap	$B_\theta = \frac{\mu_0 I_0}{2\pi r}$	$\varepsilon = 0.8$, $H = 30\,W\,m^{-2}\,K^{-1}$
14. Ingot air	$B_\theta = \frac{\mu_0 I_0}{2\pi r}$	$\varepsilon = 0.8$, $H = 50\,W\,m^{-2}\,K^{-1}$
15. Ingot bottom	Zero flux	$T = 800$ K

Table 3. Averaged material properties and operation parameters of the ESR process.

Material properties	Slag	Steel
Density ($kg\,m^{-3}$)	2 650	7 000
Viscosity (Pa s)	0.002	0.0062
Specific heat ($J\,kg^{-1}$)	1 250	800
Liquid thermal conductivity ($W\,m^{-1}\,k^{-1}$)	4	40
Solid thermal conductivity ($W\,m^{-1}\,k^{-1}$)	0.5	25
Thermal expansion coefficient (K^{-1})	9×10^{-5}	0.0001
Liquidus temp. (K)	1 685	1 760
Solidus temp. (K)	1 598	1 670
Enthalpy of fusion ($J\,kg^{-1}$)	475 000	260 000
Liquid electric conductivity ($\Omega^{-1}\,m^{-1}$)	120	8.8×10^5
Solid electric conductivity ($\Omega^{-1}\,m^{-1}$)	15	8.8×10^5
Mag. Perm. ($J\,m^{-1}\,A^{-1}$)	$4\pi \times 10^{-7}$	$4\pi \times 10^{-7}$
d_1 (μm)	–	300
k_p	–	0.35
T_f (K)	–	1811
Operation parameters		
Ingot diameter (m)	0.75	
Electrode diameter (m)	0.5	
Slag height (m)	0.15	
Melt rate ($kg\,h^{-1}$)	750	
RMS current (kA)	14.1	
AC frequency (Hz)	50	
Power (MW)	0.75	

electromagnetic field is ignored. As a result, the electromagnetic field can be obtained independent of the influence of other fields, such as temperature or flow, making the 3D calculation feasible. As shown in Figure 1b, the magnetic field is computed in a 2D axisymmetric domain including an electric conductive mold based on the electromagnetic induction equation (B_θ). Then, the calculated parameters, such as Lorentz force and Joule heating, are interpolated and patched in the azimuthal direction within our 3D domain. Furthermore, the 2D axisymmetric computational domain and boundaries, which were also used in our previous study,[16] are shown in Figure 1a. Note that the boundary conditions of the 2D axisymmetric and 3D domains are the same. A total number of 1.85 million mesh elements are used for the 3D calculation. The calculation requires three weeks using a multi-CPU cluster (24 cores, parallel computing).

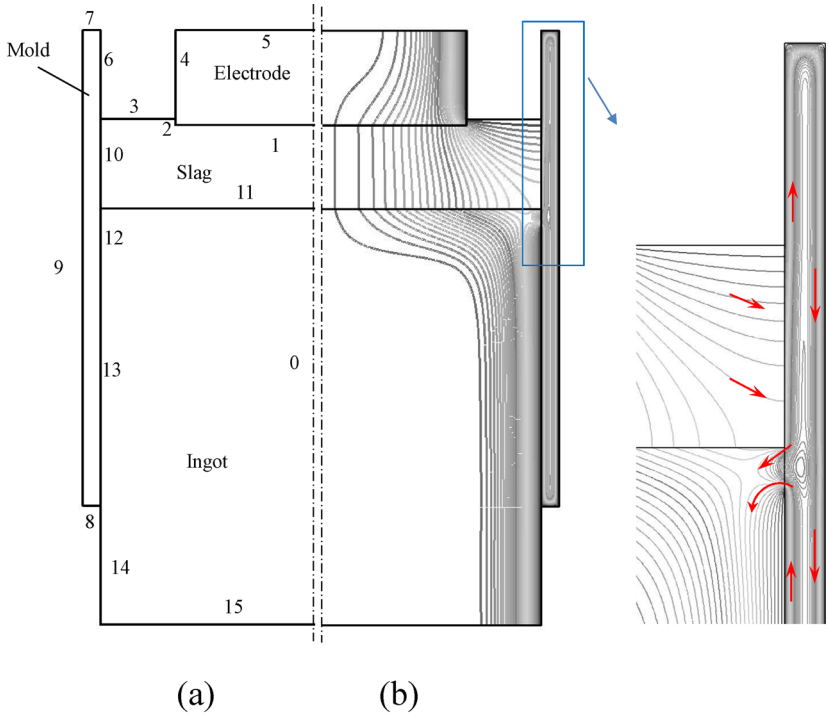

Fig. 1. (a) Computational domain and labeled boundaries. (b) Electric current path (red arrows indicate the direction of electric current).

Following the industrial process, an alternating current (AC) with a frequency of 50 Hz was applied. According to plant observations, a relatively uniform layer of slag skin (≈1 mm) developed between the solidified shell of the ingot and the mold. Electrical and thermal effects of the slag skin layer are included in the model. A portion of the electric current (≈30%) crosses the slag skin layer, entering the mold. The electric current tends to flow along the surface because of the electric skin effect. This behavior of electric current is demonstrated in the electrode, ingot, and mold (Figure 1b). As the electric current passes through the slag–pool interface, the current lines bend toward the mold. Furthermore, a strong skin effect is observed in the mold as a result of the large electrical conductivity of the copper mold ($\approx 4 \times 10^7\ \Omega^{-1}\,m^{-1}$). The eddy currents generated within the copper mold can

ADVANCED ENGINEERING MATERIALS

propagate to the steel ingot in the region where full contact (≈3 cm) is assumed between the mold and the ingot.[17]

The governing equations for the flow are solved in 3D within the slag and melt pool, including the ingot mushy zone. The thermal buoyancy is modeled with the Boussinesq approximation. The interdendritc flow in the mushy zone is modeled based on Darcy's law. The anisotropic permeability of the mushy zone according to Heinrich and Poirier[18] is applied to account for the drag resistance of the mushy zone to the interdendritic melt flow. It is considered that primary dendrites grow in the direction of the temperature gradient inside the mushy zone, thus the unit vector ($\vec{n}_{||} = \frac{\vec{T}}{\|\vec{T}\|}$) determines the parallel direction relative to the primary dendrites. The velocity ($\vec{u}_r$) of the interdendritic melt relative to dendrites can be expressed as the sum of parallel and perpendicular velocities ($\vec{u}_r = \vec{u}_\perp + \vec{u}_{||}$). After calculating the parallel velocity using the parallel unit vector ($\vec{u}_{||} = (\vec{u}_r \cdot \vec{n}_{||})\vec{n}_{||}$), one can simply obtain the perpendicular velocity relative to dendrites ($\vec{u}_\perp = \vec{u}_r - \vec{u}_{||}$). Similarly, the unit vector in perpendicular direction can be obtained: $\vec{n}_\perp = \frac{\vec{u}_\perp}{\|\vec{u}_\perp\|}$. Eventually, the calculated unit vectors are used to determine the drag resistance force (Table 1).

The turbulence is modeled using the scale-adaptive simulation (SAS) approach,[19] which is an improved version of the shear stress transport (SST-K-ω) turbulent model.[20] The accuracy of the results using the SAS model is comparable to that using the LES model with the advantage of lower computational cost.[19] The effects of droplets are considered as momentum, energy, and mass carries that impact both the slag and liquid melt pool.[21] The temperature fields in the slag, mold, and ingot are determined by solving an enthalpy conservation equation considering the source of Joule heating and solidification latent heat.[16] We treat the steel as an effective binary Fe–C alloy in which the alloy element C is very diffusive in both liquid and solid states. Thus, the Lever rule is applied to compute the liquid fraction as a function of temperature.

A transient simulation is made, and a quasi-steady state can be achieved. Snapshots of the 3D temperature field on the slag surface within a period of fifty seconds are shown in Figure 2. The flow is very chaotic and spatially disordered. The instantaneous velocity components ($u_i, i = r, \theta, z$) in radial (r), axial (z), and tangential (θ) directions can be decomposed to mean ($\bar{u}_i, i = r, \theta, z$) and fluctuating ($u'_i, i = r, \theta, z$) values aimed at characterizing the turbulent flow in the slag and melt pool. Then, distributions of the fluctuations of velocity components about the mean values are analyzed. For the latter, variances of velocity components $(\frac{1}{N}\sum_{n=1}^{N}(u_i - \bar{u}_i)^2, i = r, \theta, z)$ are calculated over a long period of time (≈30 min) until statistical invariance is achieved. Note that N is the total number of samples (≈18 000), which were obtained every 0.1 s over a total of 30 min. As shown in Figure 3, distributions of all of the components show considerable fluctuations in the same area under the electrode and near the interfaces (slag–pool or slag–air). However, the flow is almost statistically invariant near the mold wall and deep into the melt pool. Nevertheless, fluctuations are observed to be fairly axisymmetric as shown

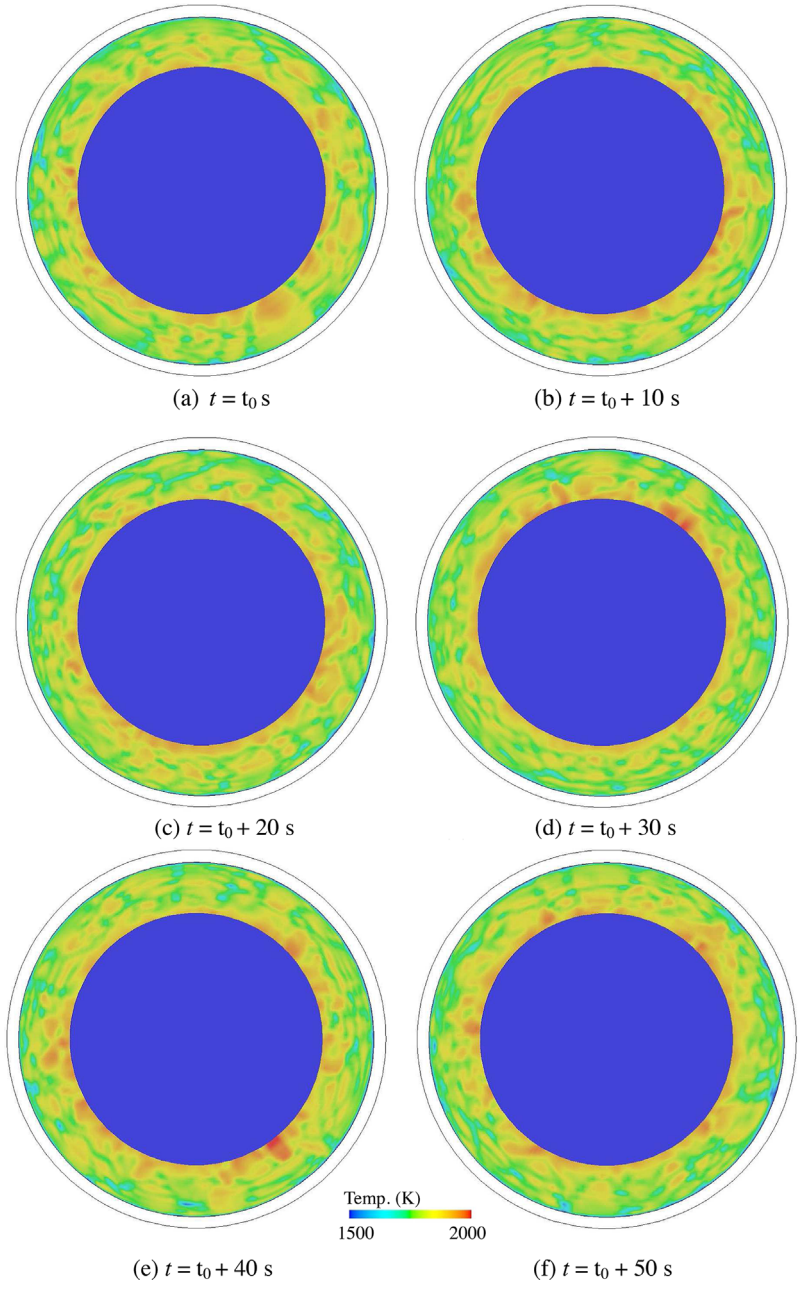

Fig. 2. Snapshots of temperature distribution on the slag free surface.

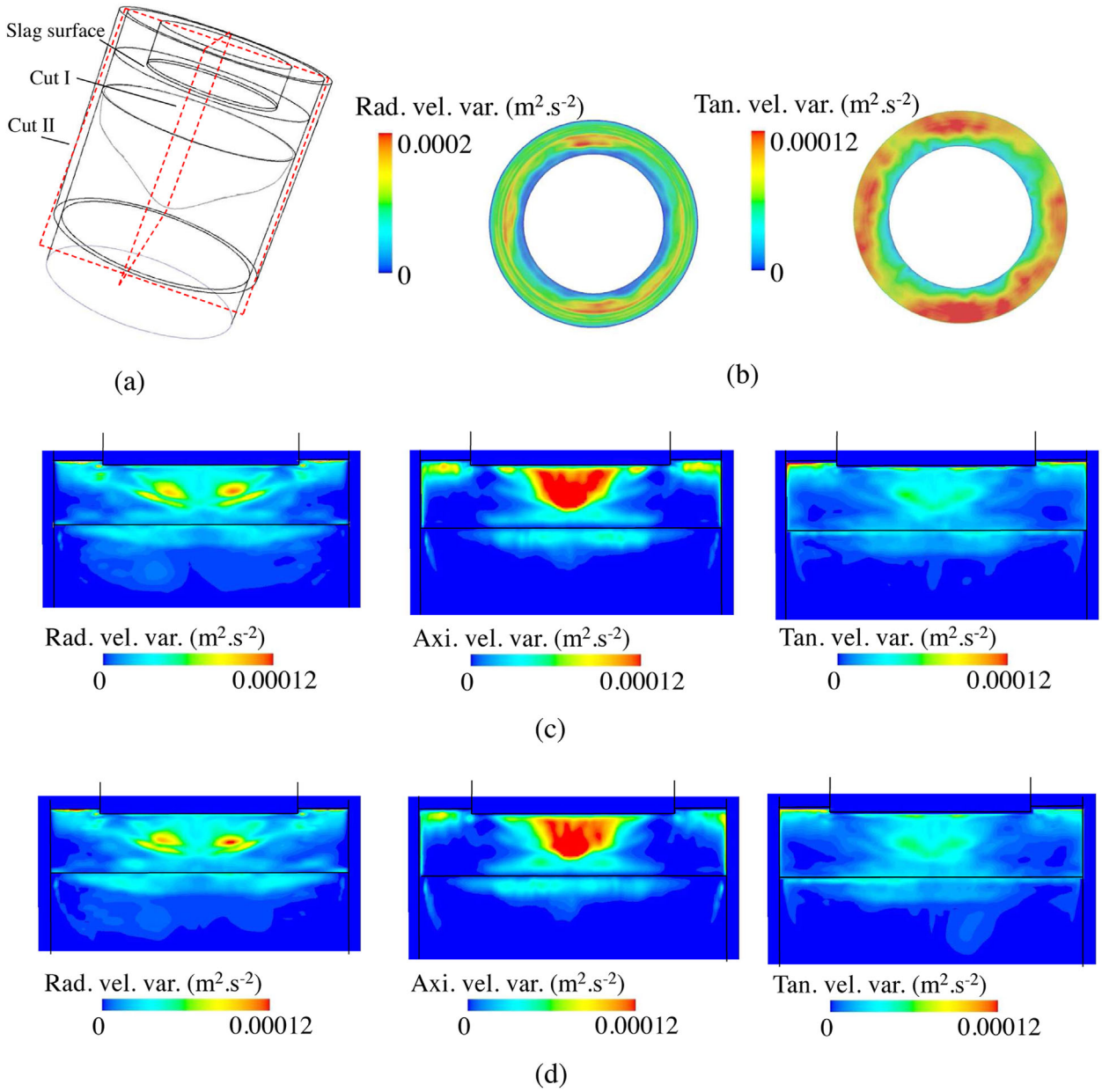

Fig. 3. (a) Demonstration of cross-sectional cuts in the 3D computational domain; (b) distribution of variance of velocity components (radial and tangential) on slag surface; (c) distribution of variance of velocity components (radial, axial, and tangential) on Cut I; and (d) distribution of variance of velocity components (radial, axial, and tangential) on Cut II.

in different sections (Cut I and Cut II) in Figure 3c–d. This result implies that a 2D axisymmetric model might be able to predict the flow behavior.

The mean velocity and mean temperature fields averaged over 30 min are also shown in Figure 4. The flow direction is drawn under the shadow of the electrode in the slag zone. It is found that the hot melt in the melt pool under the electrode is continuously pushed toward the mold wall. The flow is dominantly driven by buoyancy in the melt pool. The hottest zone in the slag zone is observed under the electrode where the current density is the largest. The turbulence in the slag is strong under the electrode region where the flow is swirling. The effective thermal conductivity in the slag bulk is dramatically increased ($\approx 80\,W\,m^{-1}\,K^{-1}$) because of the turbulence.[2] Furthermore, strong turbulence is observed in the melt pool where the effective thermal conductivity is predicted to be as large as $150\,W\,m^{-1}\,K^{-1}$. Therefore, the heat transfer is mainly governed by turbulent diffusion rather than mean flow convection in the melt pool. Essentially, the heat transfer is very efficient in the melt pool.

Despite the transient 3D flow, the pool profile is firmly steady. The kinetic energy of the melt pool ($\approx \iiint \frac{1}{2}\rho f_l \| \vec{u} \|^2$) is continuously tracked. Eventually, a weak oscillation around the average value ($\approx 0.08\,J$) is observed, demonstrating that the system reaches a quasi-steady state. It must be considered that the kinetic energy in the system might be underestimated

ADVANCED ENGINEERING MATERIALS

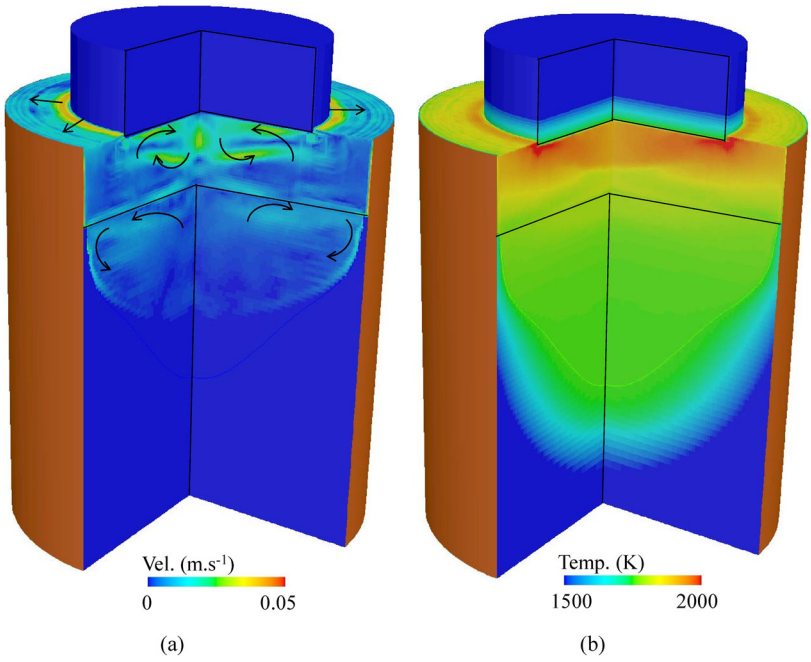

Fig. 4. (a) Mean velocity field, and (b) mean temperature field averaged over 30 min.

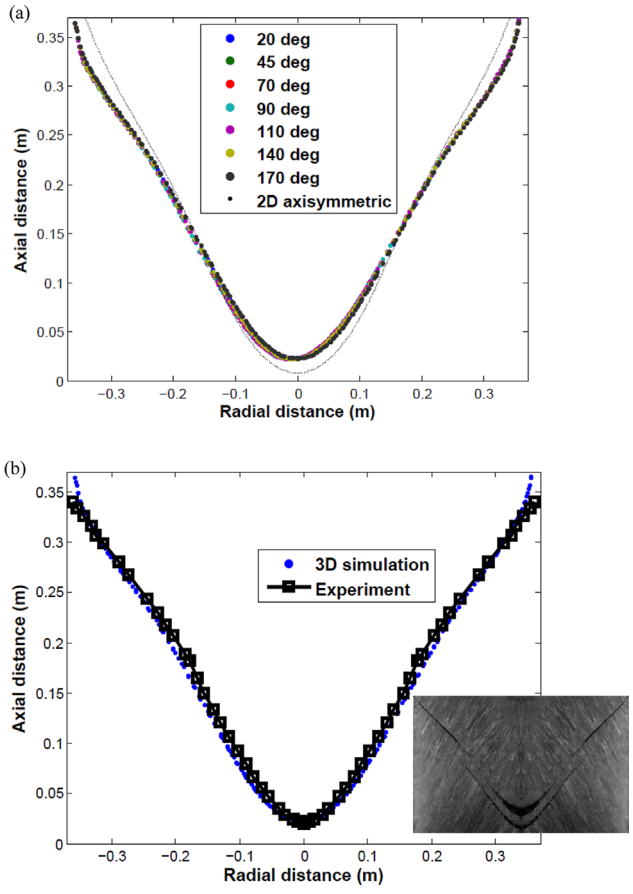

Fig. 5. (a) Pool profile obtained in various angular vertical sections of 3D simulation compared with 2D axisymmetric simulation. (b) Comparison between the simulation (3D) and experimental pool profile.

because the interface movement is not included in the current simulation.[8]

For comparison, a 2D axis symmetrical calculation with the same numerical model was performed.[16] The pool profile predicted by the 2D calculation is compared with that predicted by the 3D calculation (Figure 5a), in which an insignificant difference is observed. However, a better agreement in the shape of the melt pool is observed between the 3D simulation and the experimental results as shown in Figure 5b. In the experiment, the pool profile of the ingot defined by $f \approx 0.98$ was marked using solid tungsten granulate markers (Figure 5b). The conditions of the experiment were presented in detail by Korp and Kubin.[22]

No markers were found in the region close to the mold wall where liquid metal is in direct contact with the mold, known as the standing height or liquid cap. The length of the standing height (typically ≈1–10 cm) depends on many factors, such as the amount of mold current, contact length, and slag–pool interface movement.[7–8]

In summary, a 3D simulation is performed to analyze the transient flow behavior of an industrial scale ESR process. The numerical model includes the calculation of the electromagnetic field; the thermal field in the electrode, molten slag, ingot, and mold; the flow in the molten slag and melt pool regions; and the solidification of the ingot. The velocity field is very chaotic and turbulent; therefore, the heat transfer as a result of the turbulent eddy diffusion is very efficient, and the temperature distribution tends to become uniform in the melt pool. As a consequence, the melt pool profile is predicted to be axis symmetric, which indicates and verifies that a 2D axis symmetrical calculation is sufficient to model the melt pool profile. The results are validated against the experiment.

Article first published online: October 5, 2015
Manuscript Revised: September 14, 2015
Manuscript Received: July 29, 2015

[1] B. Hernandez-Morales, A. Mitchell, *Ironmak. Steelmak.* **1999**, *26*, 423.
[2] M. Choudhary, J. Szekely, *Ironmak. Steelmak.* **1981**, *5*, 225.
[3] A. Jardy, D. Ablitzer, J. F. Wadier, *Metall. Trans.* **1991**, *22*, 111.
[4] K. M. Kelkar, J. Mok, S. V. Patankar, A. Mitchell, *Phys. IV France* **2004**, *120*, 421.
[5] A. Patel, in *Proc. of Liquid Metal Processing and Casting*, Nancy **2007**, p. 95.
[6] A. Kharicha, A. Ludwig, M. Wu, *Mater. Sci. Eng. A* **2005**, *413*, 129.

[7] A. Kharicha, W. Schützenhöfer, A. Ludwig, R. Tanzer, M. Wu, *Steel Res. Int.* **2008**, *79*, 632.
[8] A. Kharicha, M. Wu, A. Ludwig, M. Ramprecht, H. Holzgruber, in *CFD Modeling and Simulation in Materials Processing* (Eds: L. Nastac, L. Zhang, B. G. Thomas, A. Sabau, N. El-Kaddah, A. C. Powell, H. Combeau), Wiley, New Jersey **2012**, p. 139.
[9] A. Kharicha, W. Schützenhöfer, A. Ludwig, R. Tanzer, M. Wu, *Int. J. Cast Met. Res.* **2009**, *22*, 155.
[10] A. Kharicha, A. Ludwig, R. Tanzer, W. Schützenhöfer, *Mater. Sci. Forum* **2010**, *649*, 229.
[11] V. Weber, A. Jardy, B. Dussoubs, D. Ablitzer, S. Ryberon, V. Schmitt, S. Hans, H. Poisson, *Metall. Trans. B* **2009**, *40*, 271.
[12] M. Eickhoff, N. Giesselmann, A. Rückert, H. Pfeifer, J. Tewes, J. Klöwer, in *2nd Int. Conf. on Ingot Casting, Rolling, and Forging*, Milan **2014**.
[13] K. Fezi, J. Yanke, M. J. M. Krane, *Metall. Trans. B* **2014**, *46*, 766.
[14] A. Kharicha, A. Ludwig, M. Wu, in *Proc. of EPD Congress*, San Diego **2011**, p. 771.
[15] Q. Wang, Z. He, B. Li, F. Tsukihashi, *Metall. Trans. B* **2014**, *45*, 2425.
[16] E. Karimi-Sibaki, A. Kharicha, J. Korp, M. Wu, A. Ludwig, *Mater. Sci. Forum* **2014**, *790*, 396.
[17] A. Kharicha, E. Karimi-Sibaki, M. Wu, A. Ludwig, in *Proc. of Liquid Metal Processing and Casting*, Austin **2013**, p. 95.
[18] J. C. Heinrich, D. R. Poirier, *Comptes Rendus Mecanique* **2004**, *332*, 429.
[19] F. R. Menter, Y. Egorov, in *AIAA Paper 2005-1095*, Nevada **2005**.
[20] F. R. Menter, *AIAA J.* **1994**, *32*, 1598.
[21] E. Karimi-Sibaki, A. Kharicha, M. Wu, A. Ludwig, H. Holzgruber, B. Ofner, M. Ramprecht, in *Proc. of Liquid Metal Processing and Casting*, Austin **2013**, p. 13.
[22] J. C. Korp, M. Kubin, in *INTECO Remelting and Forging Symposium*, Shanghai **2010**.

